Sensors & Actuators: A. Physical 395 (2025) 117004

Contents lists available at ScienceDirect

Sensors and Actuators: A. Physical

journal homepage: www.journals.elsevier.com/sensors-and-actuators-a-physical

Encapsulated U-shape lossy mode resonance optical fibre sensor for temperature quantification of lithium-ion batteries

Keith M. Alcock [a,*], Keng Goh [b], Mustehsan Beg [b], Sonia Melendi-Espina [a], Miguel Hernaez [a,*]

[a] School of Engineering, Mathematics & Physics, University of East Anglia, Norwich Research Park, Norwich NR4 7TJ, United Kingdom
[b] School of Computing, Engineering & the Built Environment, Edinburgh Napier University, Edinburgh EH10 5DT, United Kingdom

ARTICLE INFO

Keywords:
Lossy mode resonance
Optical fibre sensor
Energy storage
Graphene oxide
Thin-film
Lithium-ion

ABSTRACT

Accurate measurement of essential operational parameters in electrochemical energy storage devices is vital for ensuring reliable and long-lasting performance in a circular economy. This study presents the first use of a Lossy Mode Resonance (LMR) optical fibre sensor to measure the temperature of lithium-ion batteries, which is a highly influential aspect of their degradation. This technique enables an effective and simple application of optical fibre sensors for energy storage devices. The design involves using a U-shaped fibre to accurately detect changes in absorption, rather than changes in wavelength. Additionally, it incorporates a thin-film of graphene oxide and polyethyleneimine to induce the LMR which is enclosed within polydimethylsiloxane which alters refractive index with temperature. The total sensitivity reached is −0.0072 A.U./°C and −0.39 nm/°C, with excellent linearity values of R^2 0.98 and R^2 0.99 for the 2 C and 2.5 C discharge rates, respectively. This work emphasises the affordable, accurate, and innovative use of LMR sensors, which encourages the advancement and utilisation of these sensors in electrochemical energy storage systems.

1. Introduction

Electrochemical energy storage devices, such as batteries and supercapacitors, are increasingly crucial in the current energy-intensive socio-economic trajectory. There is a growing expectation that their continued advancement will assist in the fight against and reduction of global warming in the collaborative effort to address climate change. However, in order to accomplish this, these technologies must not contribute to the underlying problem and must attain longevity in order to be beneficial [1,2].

When seeking sustainable devices, it is crucial to consider the availability of resources, the environmental effectiveness, scalability, and toxicity of their production techniques, as well as their potential for recycling at the end of their useable lifespan. Currently, certain "critical materials" are vital components in significant energy conversion and storage technologies. Lithium, cobalt, and graphite are essential components of lithium-ion batteries (LIBs), which currently have a significant market share. Furthermore, vanadium serves a vital role in redox flow batteries. These factors are promoting initiatives to develop and transition to more environmentally friendly alternatives [3–5]. Nevertheless, these alternatives are currently in the experimental stage and have not yet progressed beyond the boundaries of the laboratory. Therefore, the reliability of the current generation of energy storage devices is of paramount importance due to the increasing demand and subsequent use of valuable and limited resources. Therefore, it is crucial to devise sensing methods that can effectively monitor crucial variables to enhance their durability prior to their eventual recycling in a circular economy.

LIBs are commonly used in many applications, such as mobile phones, portable computers, wearable and medical equipment, and more recently, electric vehicles. The electric vehicle sector is a significant catalyst for the increased adoption of LIBs. According to the International Energy Agency's most recent global electric vehicle outlook report, the automotive sector experienced a 65 % surge in demand for LIBs in 2022, reaching a total of 550 GWh [6].

The longevity of LIBs is influenced by various causes with elevated temperature being particularly significant. High temperature triggers several degradation mechanisms, such as the formation and decomposition of the Solid Electrolyte Interphase (SEI) layer, as well as the degradation of electrolyte and binder materials [7,8]. It is crucial to

* Corresponding authors.
E-mail addresses: k.alcock@uea.ac.uk (K.M. Alcock), m.hernaez@uea.ac.uk (M. Hernaez).

https://doi.org/10.1016/j.sna.2025.117004
Received 29 April 2025; Received in revised form 2 August 2025; Accepted 24 August 2025
Available online 26 August 2025

address the factors influencing the growth/breakdown of the SEI layer and electrolyte, as they can result in the depletion of lithium inventory [7]. Additionally, binder decomposition can lead to the loss of active anode and cathode materials resulting in power and capacity reduction of the device [7]. The ideal operating temperature range for a LIB lies between 15 °C and 35 °C [9]. To maintain this temperature range, the Battery Thermal Management System (BTMS) is utilised to monitor and control temperature variations within battery packs [10]. However, temperature quantification typically is not taken at the individual cell level, but rather at a single point for a group or 'module' of cells. In addition, the temperature monitoring is owed to the wiring requirements of traditional temperature measuring devices, such as thermocouples [11], thus limiting the data accessible to the BTMS [11]. Hence, it is crucial to establish real-time temperature monitoring of LIBs to implement proactive maintenance, which will result in an extended battery life and reduced downtime. The resulting effects encompass decreased costs, enhanced customer satisfaction, and a distinct advantage in the marketplace.

Optical fibre sensors are becoming a popular approach for measuring a multitude of battery parameters since they offer clear benefits compared to traditional sensing methods [12–14]. These sensors utilise the characteristics of light transmission through optical fibres, providing advantages, such as high precision, immunity to electromagnetic interference, small size, durability in harsh environments and multiplexing capabilities [15,16]. Accordingly, the high interest that optical fibre sensors are generating for their implementation in batteries.

In this context, optical sensing systems using Fibre Bragg Gratings (FBGs) have been explored, obtaining very promising results. FBGs are conventional fibres with a distributed Bragg reflector that is inscribed in a small portion of the fibre core. This Bragg is designed to reflect a certain range of wavelengths of the guided modes while permitting all others to transmit through [16,17]. These sensors have been utilised for applications such as temperature detection [18–20], strain measurement [21–24], and dendrite formation [25] in LIBs. However there are some limitations to FBGs, for example, while collecting temperature and strain data it is necessary to distinguish between these as it is capable of monitoring both simultaneously [26]. Microtubes made of glass, metal, or polymer are commonly used in this method to enable silica glass or polymer fibres to expand and constrict, effectively separating sensing targets [27–29]. Moreover, FBGs typically require a complex and often expensive manufacturing process using a complex laser setup for FBG inscription [30] or a commercial setup, such as a Northlab Photonics Noria FBG manufacturing system [18,20,31,32] or Coherent Braggstar system [33], as well as a relatively expensive interrogation system to provide and measure the reflected wavelengths. Consequently, it is essential to find other more robust and affordable sensor platforms.

This study demonstrates that optical fibre sensors using Lossy Mode Resonance (LMR) are a viable substitute for FBGs in electrochemical energy storage devices. An optical fibre is composed of a glass core that serves as the waveguide and a cladding material with a lower refractive index, which is used to confine the transmitted light within the core. This sensing technology utilises a thin-film material applied onto the core of the optical fibre instead of the cladding, enabling the passing of light modes into the deposited layers. In this case, the chosen thin-film material is carefully engineered to permit the transmission of light and generate an LMR. Thin-film coatings that induce LMR must demonstrate a higher and positive real component of permittivity in comparison to its imaginary component. Furthermore, the real part of the thin-film permittivity should be positive and greater in magnitude than its own imaginary part, and also greater than the real part of the permittivity of both the optical waveguide and the external medium surrounding the thin-film [34]. When these criteria are fulfilled, certain modes are transmitted to the thin-film, leading to the emergence of a detectable absorption peak. Moreover, this observed peak is highly sensitive to variations in the refractive index (RI) of the LMR generating coating as well as the surrounding environment. Therefore, the observed peak shifts towards higher or lower wavelengths when the RI increases or decreases, resulting in a highly versatile sensing platform. LMR sensors provide a broad spectrum of thin-film material options exploiting metal oxides [34–36], polymers [37–39], and graphene derivatives [40–42]. Instruments based on LMR have been developed for a diverse range of applications, including but not limited to biosensors [43,44], refractive index [45,46], chemical [47–49], humidity [50,51], pH [37,52], and gas [41,53–55] sensing. Electrochemical energy storage is an uncharted territory for LMR sensors, yet their versatility makes them an attractive alternative sensing strategy.

Fibre geometry plays a crucial role in the operation and sensitivity of LMR optical fibre sensors. Commonly, LMR sensors are implemented using straight fibre geometries, where the interaction between the guided light modes and the thin-film coating on the fibre core are relatively uniform. In these straight-type LMR sensors, resonance wavelength shifts serve as the primary sensing metric, providing clear and reliable detection of changes in external parameters such as refractive index [38,56]. However, when the fibre is shaped into a U configuration, the pronounced curvature increases the overlap between the evanescent field and the deposited thin-film, heightening propagation losses. This translates to more significant changes in absorbance or transmission loss, rather than wavelength shifts, and makes U-shaped LMR sensors particularly sensitive for certain applications [57,58]. This characteristic allows the use of more cost-effective components, such as spectrometers with a narrower wavelength range. Additionally, this setup enables a 'probe'-style device where both the input and output fibres are located on the same side of the sensor, making the overall device more practical and easier to deploy in real-world applications.

This work presents the first application of the LMR phenomenon in the context of electrochemical energy storage devices, specifically developing an LMR optical fibre sensor for *in-situ* temperature measurement within a LIB. Diverging from the typical use of straight-fibre LMR sensors, this work utilises the U-shaped geometry to exploit the heightened sensitivity of absorption shifts, allowing for the use of a lower cost micro-spectrometer with a reduced wavelength detection range.

The LMR effect is achieved with a thin-film consisting of Graphene Oxide (GO) and Polyethylenimine (PEI), deposited using a dip assisted Layer by Layer (LbL) methodology. The sensor further comprises an encapsulant made of Polydimethylsiloxane (PDMS). The PDMS is implemented as it exhibits a shifting refractive index with temperature [59–61], thereby affecting the absorption peak of the LMR generating thin-film. This study demonstrates the successful utilisation of LMR optical fibre sensors for the measurement of temperature, a crucial factor in electrochemical energy storage. The cost-effectiveness of these sensors as a viable alternative to the complex and expensive FBGs is underscored by the use of less complicated manufacturing and cheaper setup. The primary goal of this investigation is to encourage the development of cutting-edge optical sensors that employ LMR for electrochemical energy storage. The sensing strategies for applications such as LIBs have the potential to be revolutionised by these sensing devices, which will ensure their reliable and long-lasting performance. This, in turn, will facilitate the development of a circular economy that is sustainable and necessary for the future.

2. Materials and methods

2.1. Materials

The U-shaped sensor utilised the FT200EMT multimode optical fibre (Thorlabs Inc.) which consisted of a 200 μm silica glass core with a numerical aperture of 0.39 with a hard clad TECS™ polymer coating and a Tefzel buffer. The GO dispersion was sourced from GO Graphene UK, while PEI was sourced from Sigma Aldrich UK. The GO dispersion and PEI solution were diluted to final concentrations of 0.5 mg/mL and 2 mg/mL using 18.4 Ω water. Their pH values were measured as 5.2 and

8.3, respectively. The PDMS was acquired from Sigma Aldrich, UK, in the form of 'SYLGRD® 184' 5 g clip packs.

2.2. Sensor fabrication

2.2.1. U-shape fabrication

Fig1 depicts the U-shaped structure of a fibre, where the U-shape was measured to be 1.6 mm in diameter with a total exposed core length of 7.1 mm. The U-shape's diameter was selected based on the published optimum diameter of 1.5 mm [62]. Any diameter below this value results in reduced sensitivity, therefore, the diameter was produced as near to 1.5 mm as possible.

The fabrication procedure of the U-Shaped optical sensor began with selecting an 80 cm segment of optical fibre. Approximately 25 mm of the Tefzel outer buffer was removed from both ends and the core cleaved with a NorthLabs ProCleave LD II large diameter fibre cleaver, allowing both ends ready for connecting to the spectrometer and light source. Next, at the 40 cm point, a stripping tool was employed to separate and pull one side of the remaining buffer, creating an opening in the Tefzel buffer. Once the stripping tool was removed from the fibre, the Tefzel buffer was carefully adjusted to provide the required space. A 5 mm section of the fibre core was revealed using this method. After the buffer gap was established, the fibre was firmly secured to the work bench and held taut, and a butane flame was employed to remove the TESC™ polymer cladding from the fibre core. Subsequently, the fibre was held in the air and allowed to bend into a curved configuration. Following that, the butane flame was swiftly directed towards the centre of the exposed core area. As the core underwent heating, a gradual and permanent curvature in the fibre was induced. The heating procedure was iterated several times until the desired curvature was achieved. It is important to note that while utilising the initial butane flame to remove the tough polymer cladding, a portion of the Tefzel buffer that remained was reduced, leading to a larger exposed area. Hence, it was crucial to factor in this aspect while striving to achieve an exact exposed core length. Furthermore, this procedure guaranteed the secure fastening of the buffer to the core by the act of melting the end, thus establishing a seal between the buffer and the core, as can be seen in Fig. 1.

Finally, the U-shaped fibre was exposed to sonication in acetone for a period of 30 min to remove any residual cladding and residue from the core. Afterwards, the fibre was exposed to sonication in deionized water with detergent for an additional 30 min to ensure the thorough elimination of acetone, then meticulously rinsed with distilled water and allowed to air dry. Finally, the fibre was thoroughly cleaned in anticipation of the LbL thin-film deposition.

2.2.2. LMR generating thin-film

The PEI/GO LMR thin-film was deposited by means of dip assisted LbL, which is published elsewhere [50,63–65]. The process, summarised in Fig. 2 used a GO dispersion with a concentration of 0.5 mg/mL and a PEI solution with a concentration of 2 mg/mL. To begin with, the U-shaped fibre section was immersed in a potassium hydroxide solution (1 M) for a duration of 30 min to acquire a negative charge. Afterwards, the fibre was washed with deionized water and then allowed to air dry for 1 min. The negatively charged fibre was then submerged in a solution containing positively charged PEI for a duration of five minutes. Following that, the fibre underwent a further rinsing process using deionized water, which was followed by drying in air. Subsequently, the fibre was immersed in the GO dispersion, which had a negative charge, for an additional five minutes. Once the fibre was rinsed with deionized water to eliminate any remaining dispersion, it was left to air dry. This process was repeated for the deposition of 3 bilayers, resulting in a thin-film of approximately 46 nm thickness [65].

2.2.3. PDMS encapsulation and sensor packaging

The U-shaped fibre with PEI/GO, was encapsulated with PDMS. The PDMS is temperature-sensitive, meaning that its refractive index changes with temperature. This change in refractive index affected the response of the thin-film which induced the LMR. The method of encapsulating entailed using a Phrozen Sonic Mini 8 K printer together with the necessary washing and curing stations to create a protective casing. The enclosure was designed with a removable concave wall to match the curvature of the INR18650MJ1 lithium-ion cells used in the experiments, and a cylindrical void with a diameter of 5 mm. Adhesive tape was used to secure the detachable wall to the casing, facilitating the pouring and moulding of the PDMS. The PDMS mixture was poured into the casing and then placed inside a vacuum chamber for a period of 10 min to remove any significant bubbles. Afterwards, the U-shaped fibre was carefully inserted into the case that contained the liquid PDMS and left overnight in a drying oven set at 40°C to ensure complete curing of the PDMS.

An exploded view of the fibre sensor assembly is depicted in Fig. 3a. This view shows the U-shaped fibre which is inserted into the PDMS

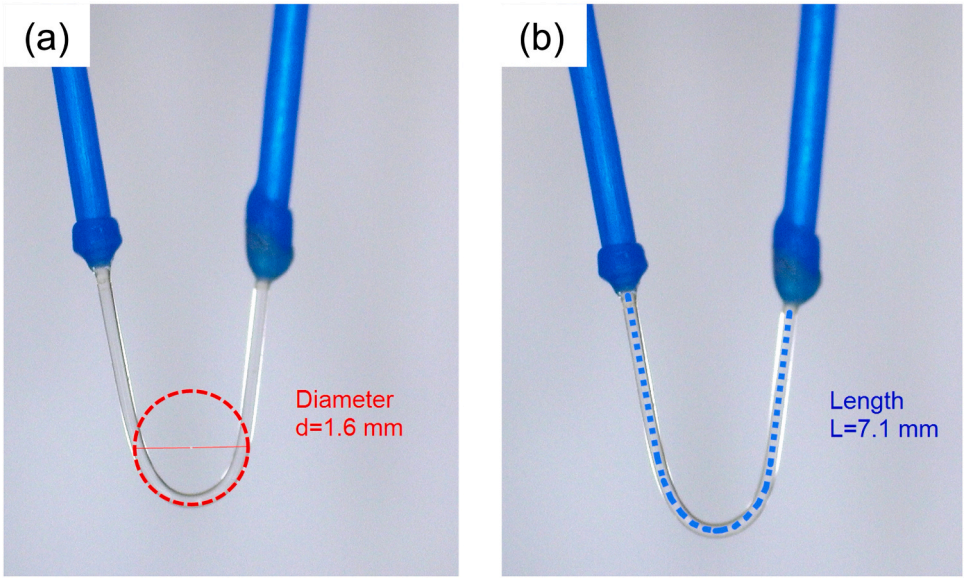

Fig. 1. Sensor design and fabrication (a) U-Shape fibre sensor diameter measurement showing 1.6 mm, (b) U-Shape fibre sensor exposed core length for thin film deposition, length of 7.1 mm.

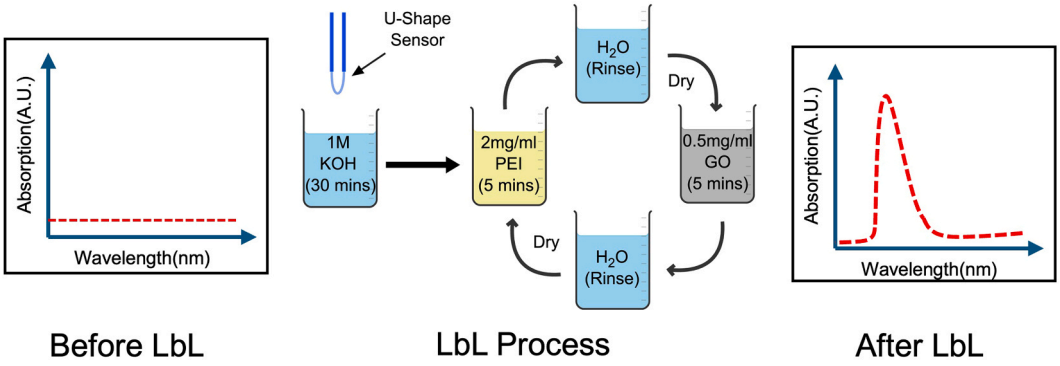

Fig. 2. Layer by layer process on U-shape sensors, illustrating thin-film absorption before and after the deposition process.

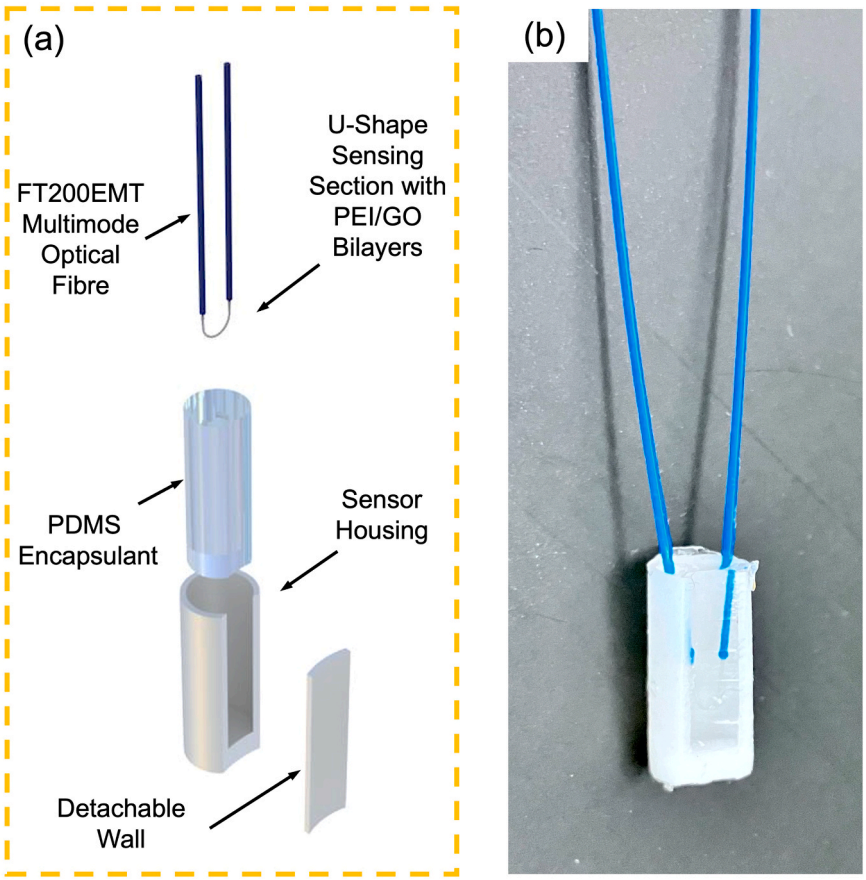

Fig. 3. (a) Exploded illustration of the sensor components, showing the U-Shape fibre with exposed sensor section, PDMS encapsulant, cell housing and the detachable housing wall used during PDMS curing process, and, (b) Final fabricated U-Shape encapsulated optical fibre sensor.

encapsulant that was contained within the sensor housing. In order to ensure that the sensor assembly was able to rest firmly on the curve of the cylindrical LIB, the housing was purposefully developed to feature a concave surface.

The detachable housing wall was used in the PDMS curing process allowing for a contact area of 35.11 mm^2 post curing. The completed device, which is seen in Fig. 3b, offers a sturdy container for the fragile silica glass fibre core, which was safeguarded by a functional PDMS encapsulant responsible for stimulating the LMR generating thin-film. Additionally, the encapsulant serves as protective barrier against moisture due to its high hydrophobicity, thus rendering the sensor stable in respect to fluctuating humidity [66].

2.3. Experimental

2.3.1. Setup

Fig. 4a depicts an overview of the experimental configuration in which the lithium-ion cell was placed within a controlled environment by means of an ESPEC LU-114 temperature chamber that was set at 25 °C with a tolerance of ±1 °C. This configuration ensured a consistent and reliable environment for validating the experimental outcomes. The LIB was connected to a B&K Precision 8610 DC electronic load connected by a 4-wire connection. The temperature was recorded using a TC-08 thermocouple data logger (Pico Technology, UK). An Ocean Insight HL-2000 halogen light source produced light within the visible spectrum, which was then transmitted to the U-Shape fibre sensor. The light was subsequently measured at the opposite end of the fibre using

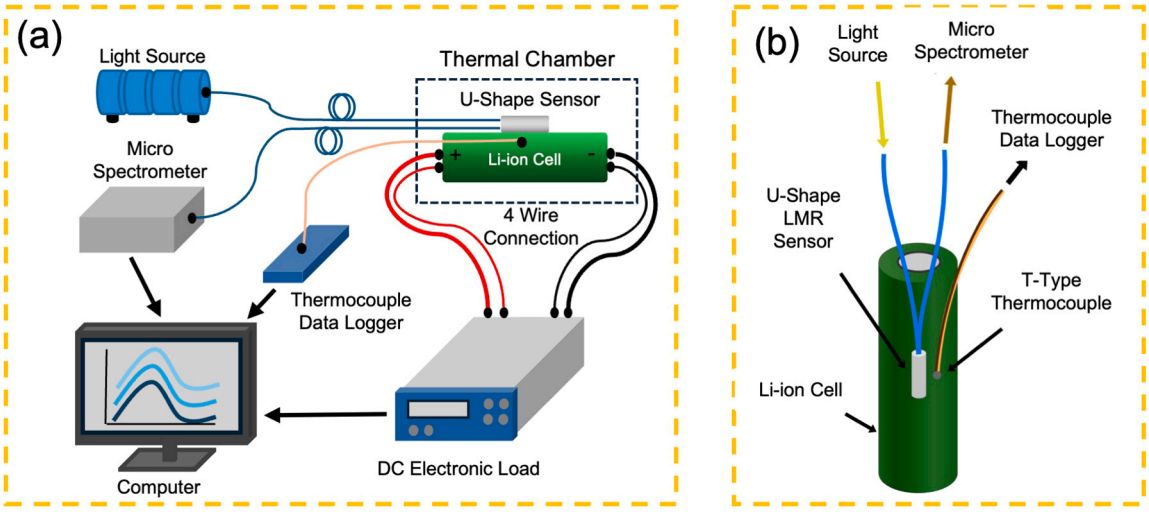

Fig. 4. Experimental Setup (a) Schematic of the experimental setup where the Li-ion cell is contained in a thermal chamber at 25 °C ± 1 °C and connected via a 4-wire battery holder, and (b) Schematic of the sensor placement on the Li-ion cell.

an Ocean Insight ST-VIS-25 micro spectrometer, a relatively inexpensive device that functioned in a wavelength range of 350 nm to 810 nm and possessed an optical resolution of 2.2 nm.

Fig. 4b depicts the placement of the sensors on the INR18650MJ1 cylindrical lithium-ion cell. The spectrometer, electronic load and TC-08 were linked to a computer for data collection. The encapsulated sensor and thermocouple were placed adjacent to each other and affixed to the cell using polyimide tape. In order to obtain accurate temperature measurements, a factory calibrated T-type thermocouple (Labfacility, UK) was utilised, which complies with the IEC 584 Class 1 standard, ensuring a tolerance of ±0.5 °C.

2.3.2. Data acquisition and analysis

The Ocean Insight Oceanview software, in conjunction with the micro spectrometer, was employed to collect spectral data from the encapsulated LMR sensor. The temperature data was acquired utilising the PicoLog software (Pico Technology, UK) from the thermocouple data logger. The LIB discharge data from the electronic load was collected using the B&K Precision battery testing software, with measurements recorded at a frequency of once per second. The temperature data from the thermocouple and the spectrum data were recorded at a frequency of one measurement every ten seconds.

The data aquired by the spectormeter was used in (1) to derive the light absorption by the LMR thin-film, where A is the dimentionless absorption unit A.U., I_0 is the reference spectrum recorded before thin-film deposition,and,I is the logged spectrum after thin-film deposition during the experimental process.

$$A = \log_{10} I_0/I \tag{1}$$

The equation was applied to each spectrum recorded at 10-second intervals to calculate the LMR peak. To accurately determine the maximum point of each LMR curve, a third order polynomial approximation was employed due to the noise in the LMR peak. This was accomplished by employing a MATLAB process, as the dataset for each experiment was substantial, necessitating an automated procedure.

3. Results and discussion

3.1. Battery discharge response

The lithium-ion cell was subjected to three different discharge conditions: 1 C, 2 C, and 2.5 C. These conditions correspond to constant current loads of 3.4 A, 6.8 A, and 8.5 A, respectively, which does not exceed the maximum continuous discharge rating of 10 A for the INR18650MJ1 lithium-ion cell. The initial voltage of each cell, measured in an open circuit condition before discharge, was found to be 4.181 V, 4.183 V, and 4.178 V for discharge rates of 1 C, 2 C, and 2.5 C correspondingly. Exhibiting a maximum deviation of 5×10^{-3} Volts. Fig. 5a shows the decrease in voltage of the cells caused by the discharge load, displaying a voltage drop which increases from 0.151 V at 1 C to 0.334 V at 2 C and 0.346 V at 2.5 C (Fig. 5a Subplot). The duration of each discharge test varied due to the differing constant current loads resulting from the discharge conditions. The discharge rates of 1 C, 2 C, and 2.5 C result in discharge durations of 3514 s, 1754 s, and 1418 s, respectively.

As the temperature is recorded for three discharge conditions, it is crucial to recognise the initial temperature for each discharge. If this temperature is not consistent, the final results cannot be compared for sensor testing. For the three discharge conditions 1 C, 2 C, and 2.5 C the thermocouples record this temperature as 24.82 °C, 24.75 °C, and 24.57 °C, respectively. Each test started within 0.5 °C of each other, which falls within the tolerance range of the T-type thermocouple. The discharge conditions induce a temperature gradient, at the end of 1 C discharge the temperature reaches 33.14 °C, after 2 C discharge, 43.24 °C, and 47.64 °C after 2.5 C discharge. These values can be observed in Fig. 5b. As a result, there is a temperature difference (ΔT) of 8.32 °C, 18.49 °C, and 23.07 °C, for the increasing C-rates respectively.

In addition, the total capacities achieved for 1 C, 2 C, and 2.5 C are determined to be 3.315 Ah, 3.310 Ah, and 3.346 Ah, respectively (Fig. 5c). The maximum deviation observed is 36×10^{-3} Ah, indicating that the discharge results are similar, thus implying that the cells are discharging to similar levels. Ultimately this demonstrates that the LIB response is comparable and that the thermal gradients are appropriate, as the cells do not show any significant degradation.

3.2. Sensor response

3.2.1. LMR thin-film response

As previously stated, the U-shape fibre was subjected to a LbL deposition process, where a thin-film was deposited using PEI and GO to generate the LMR. The thin-film assembly demonstrates an increase in absorbance in response to the addition of each bilayer, as measured by the micro spectrometer. Fig. 6 demonstrates that the absorption peak of LMR gradually increases from 0.14 A.U. for the first bilayer to 0.52 A.U. for the second bilayer, and ultimately to 0.86 A.U. for the third bilayer.

In addition, the peak wavelength undergoes a shift from 401.3 nm to

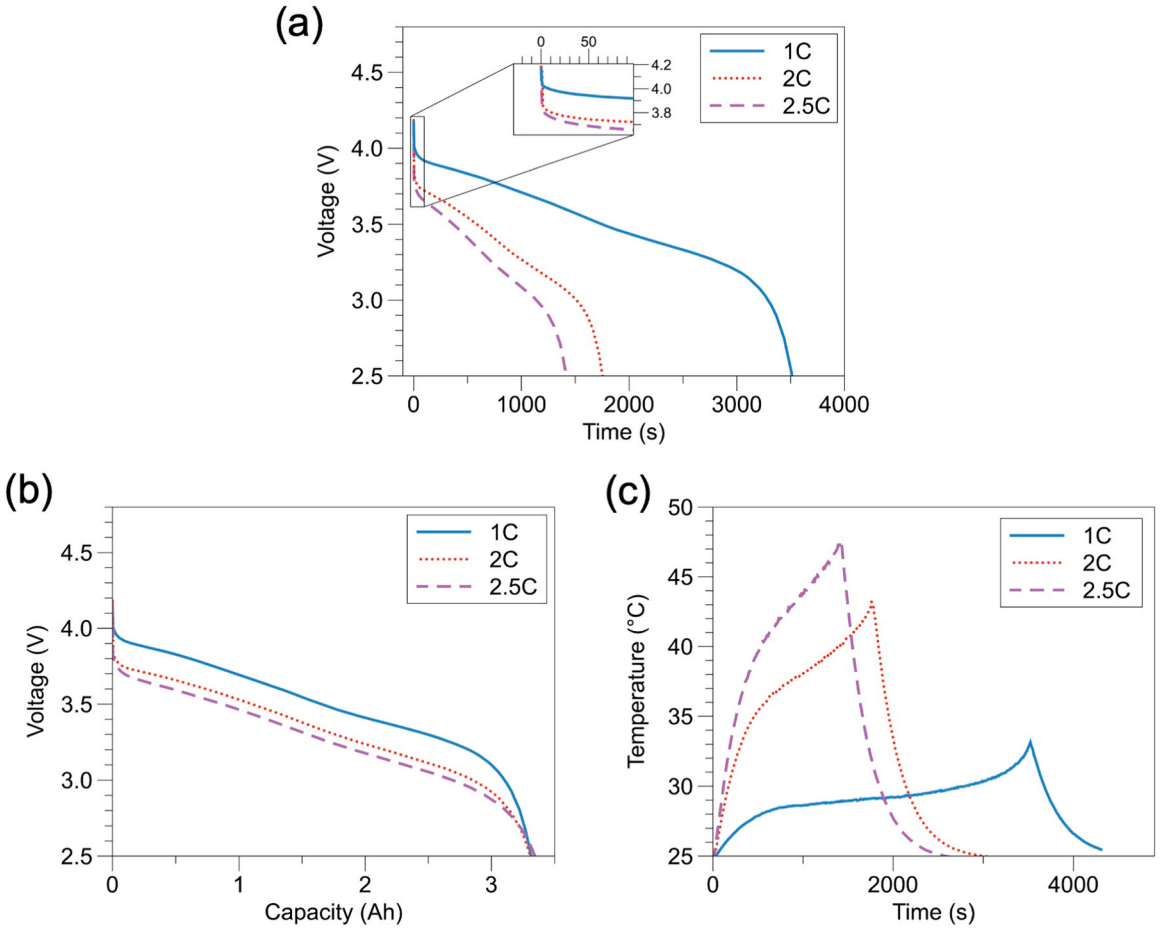

Fig. 5. Experimental Setup and Li-ion Response. (a) The voltage response to the three discharge conditions, showing increased voltage drop as the discharge rate increases. (b) The thermal response of the Li-ion cell during the three discharge conditions, showing temperature increase and cooling after discharge end, and (c) The voltage decrease and discharged capacity increase during the three discharge conditions, showing similar achieved discharge capacity for each discharge condition.

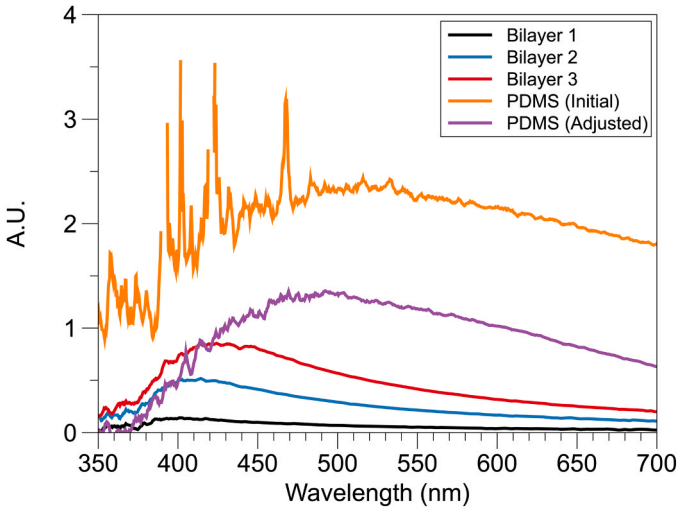

Fig. 6. Spectra graph, showing three LMR inducing bilayers, illustrating the increase in LMR induced by the addition of PEI/GO bilayers. Both the final LMR peak (purple line) from the micro spectrometer's integration time adjustment and the LMR peak in cured PDMS (yellow line) are visible.

424.14 nm as the deposition of the thin-film increases from one bilayer to three bilayers. The selection of three bilayers was determined by the existence of a distinct LMR peak that remains below 1 A.U. This is essential because the RI of the PDMS material contributes to additional peak displacement. To assess the reproducibility of the deposition process aimed at maintaining peak values below 1 A.U., three sensors were fabricated under identical conditions, and their peak values measured to calculate the mean and standard deviation. After one bilayer deposition, the average peak value was 0.13 with a standard deviation of 0.008; after two bilayers, the average peak increased to 0.496 with a standard deviation of 0.016; and following three bilayers, the average peak reached 0.981 with a standard deviation of 0.09. These results demonstrate a high degree of reproducibility and reliability in the LbL deposition process, as indicated by the consistently low standard deviations across all bilayers.

Once the fibre is encapsulated in the PDMS and allowed to cure, the LMR curve experiences a shift and becomes noisier as demonstrated by the orange line in Fig. 6. This evidence strongly supports terminating the LbL process after three bilayers. Continuing beyond this point would result in heightened absorption, which in turn would generate increased noise and reduced light output upon encapsulation. In order to improve the quality of the LMR curve, the integration time of the ST-VIS-25 micro spectrometer was adjusted. This modification allows the linear Charged-Coupled Device (CCD) array to capture light for a longer period before it is passed to the analogue to digital converter. As a result, noise is reduced and the LMR curve appears cleaner, as indicated by the purple line in Fig. 6. This LMR curve, which was used as the basis for the testing

procedure, shows a peak value of 1.33 A.U. at a wavelength of 505.54 nm.

3.2.2. Thermal response

The LMR curve for T_{Max}, T_{Start}, and T_{Cooled} is depicted in Fig. 7a, b, and c for discharge at 1 C, 2 C, and 2.5 C, respectively. T_{start} represents the initial temperature of the LIB before starting the discharge process. T_{max} represents the highest temperature reached by the LIB, i.e., at the end of the discharge. T_{Cooled} refers to the temperature recorded once the LIB has cooled down to a value that was similar to the T_{start} temperature. It is clear that as each discharge occurs, the maximum absorption reduces as there is a rise in temperature, and then returns to its original position when the temperature decreases again. The decrease in absorption in the LMR peak becomes more noticeable as the temperature change is amplified. This is because the rate at which the LIB discharges is increased, as indicated by the difference between the results shown in Fig. 7a (with a lower temperature change) and Fig. 7b and c (with a greater temperature change). Thus, it is evident that the RI of the PDMS is shifting as a result of the temperature change on the LIB surface. As stated in [61] the RI reduces as temperature increases, resulting in the detectable LMR shift presented.

The presence of noise in the data depicted by these LMR curves poses a challenge in accurately determining the central peak of each curve obtained at 10-second intervals during each test. This emphasises the previously mentioned approach of using third order polynomials to accurately identify the LMR maxima in each recorded interval. Using an automated MATLAB routine, the mean R^2 value for all data points was determined to be 0.98 for both 1 C and 2 C discharge conditions, and 0.96 for the 2.5 C discharge condition.

The fluctuations observed by the encapsulated sensor, specifically the changes in peak absorption (Δ A.U.) and peak wavelength (Δ nm), along with the temperature variations of the LIB measured by the thermocouple (ΔT), are depicted in Fig. 8 displaying the complete datasets for intervals of 10 s. A similar variation in the maximum absorption and wavelength, marked by a reduction in both, is noticed as the temperature rises, and then diminishes as the LIB cools.

Visually, it is evident that the peak absorption (purple plots) demonstrates greater accuracy when compared to the peak wavelength shift (green plots). The main reason for this is that absorption shift is more prevalent in U-shaped designs compared to straight fibre LMR sensors, where wavelength shift is more pronounced [62,67]. In addition, the spectrometer utilises a CCD array with a total of 1516 active pixels. Each pixel corresponds to a detectable wavelength and records 1 point in the spectrum. However, due to the sensor design, there is only a small shift in the wavelength, resulting in a segmented range with a 'resolution' of approximately 0.3 nm. As a result, the accuracy of the Δnm response shows to be inferior than that of ΔA.U. Overall, it is clear from Fig. 8, that the U-shape design is responding well to the PDMS RI changes due to the increasing and decreasing of the LIB surface temperature, thus it is imperative to analyse the linearity of the sensor response to further assess its performance.

3.2.3. Linearity of the encapsulated sensor

The linear correlation between the sensor response and the temperature gradients induced by the LIB is shown in Fig. 9a, b, and c, specifically detailing the discharge levels of 1 C, 2 C, and 2.5 C, respectively. When examining the relationship between temperature and peak absorption, as well as the associated peak wavelength with

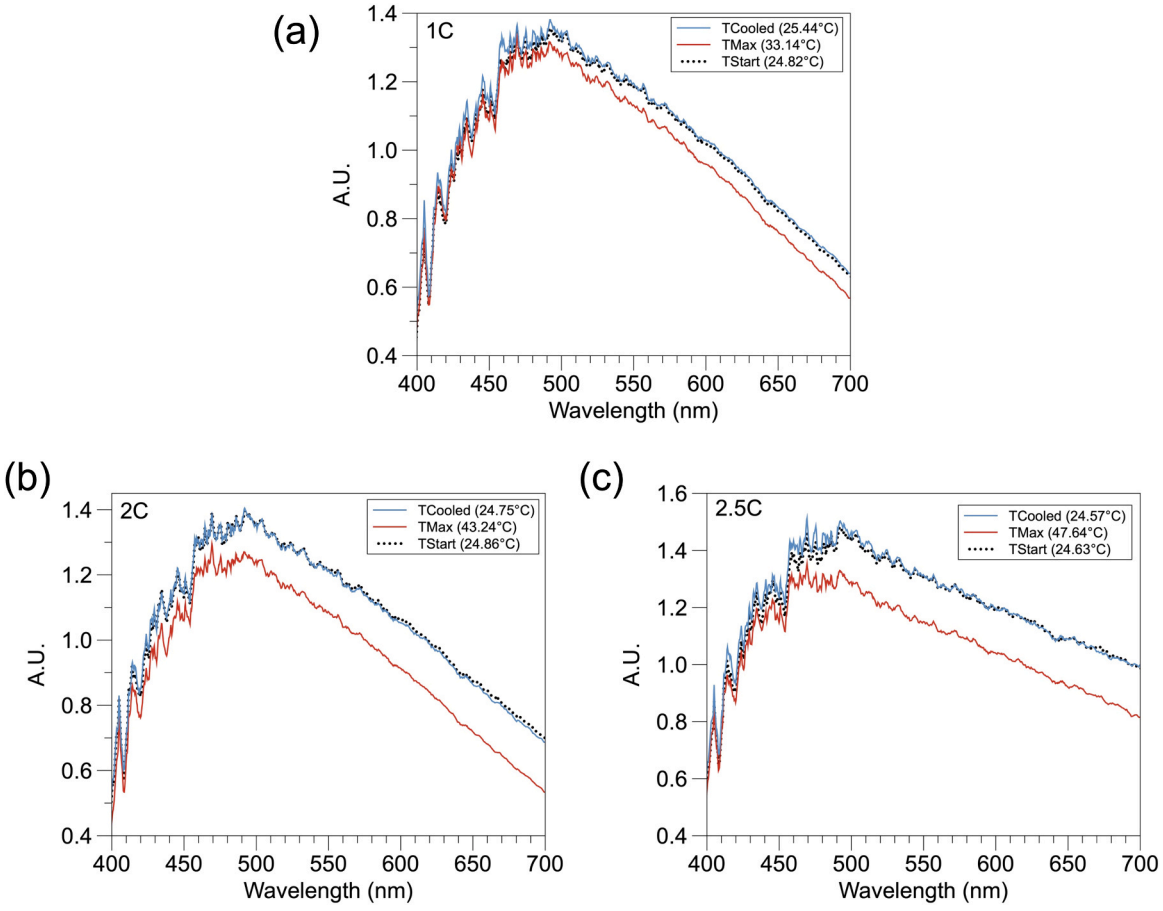

Fig. 7. The response of the LMR to changes in temperature, represented by a curve at the beginning of each test (TStart), the highest temperature reached (TMax), and the curve after the LIB has cooled down (TCooled). Showing three different discharge rates: (a) 1 C discharge, (b) 2 C discharge, and (c) 2.5 C discharge.

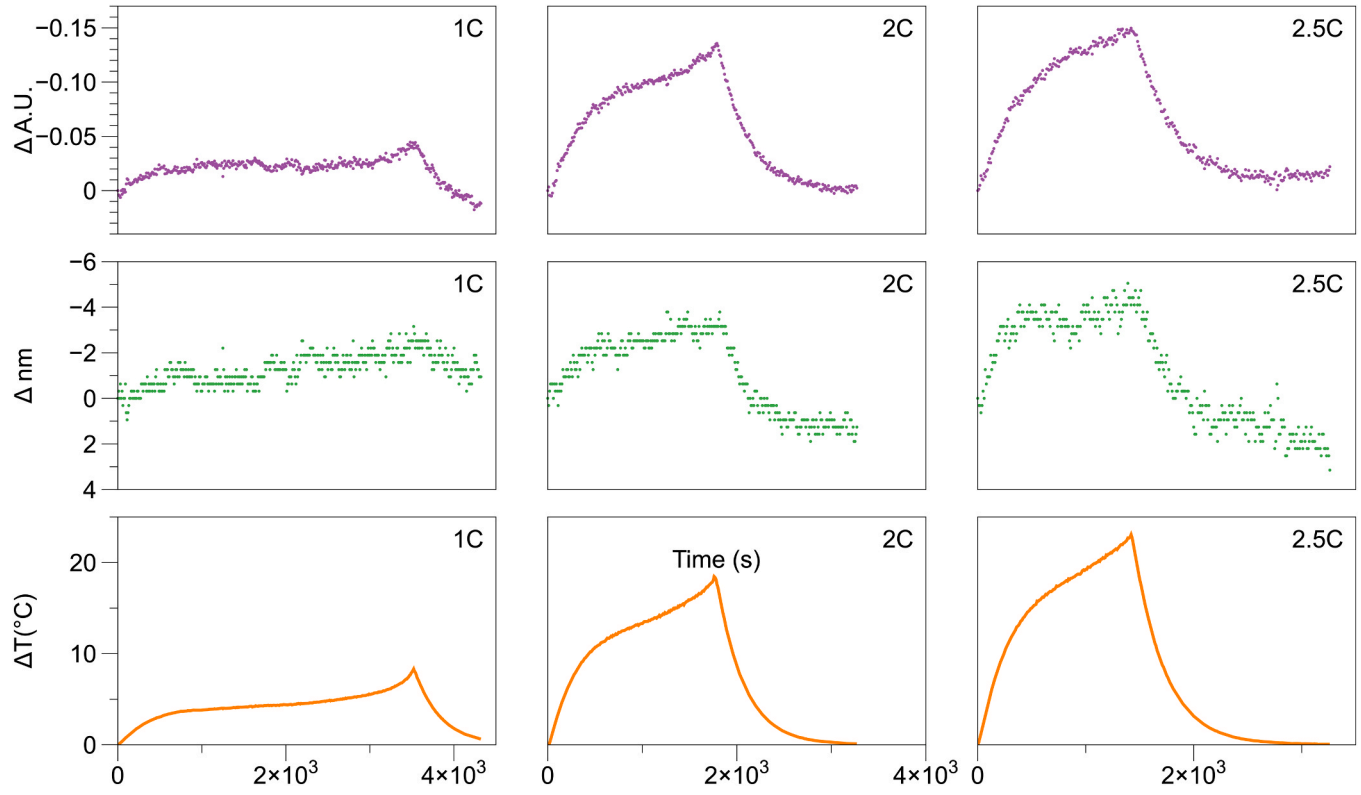

Fig. 8. The sensor's thermal response for each discharge state compared to the thermocouples. Showing ΔA.U. and Δnm calculated from third order polynomial of each curve recorded at 10-second intervals.

regard to thermocouple measurements, it becomes clear that the peak absorption demonstrates strong linearity across all discharges. Specifically, the 2.5 C and 2 C discharges demonstrate the strongest linear correlation with R^2 values of 0.98 and 0.99, respectively. The lesser R^2 value of 0.82 for 1 C indicates that the sensor is better adapted to handle a greater rate of change, the reason for this is that PDMS is reported to change RI from 1.4085 at 20 °C to 1.3907 at 60 °C in a linear fashion [61]. This shift is of minor magnitude since the 1 C discharge shows a smaller temperature variation compared to the 2 C and 2.5 C discharge conditions. Furthermore, the discharge at a rate of 1 C has a prolonged duration accompanied by a gradual rise in temperature, as depicted in Fig. 9. As a result, there is a higher concentration of data points that are closely packed together throughout the discharge, as seen in Fig. 9a at the region of Δ5 °C. The correlation of the nanometre peak, for which the R^2 is merely 0.4 for the 1 C discharge condition, in comparison to 0.89 for the 2 C and 2.5 C discharge conditions, further supports this hypothesis.

The full-scale hysteresis values obtained were 0.025 A.U., 0.014 A.U., and 0.0013 A.U. for discharge rates of 2.5 C, 2 C, and 1 C, respectively, indicating a decrease in hysteresis with smaller temperature changes. This trend is also visually evident in Fig. 9, where the gap between the cooling and heating datasets widens as the discharge rate increases.

The linear relationship formula is employed to calculate the temperature measured by the U-shaped sensor, for both the absorption peak shift and the wavelength peak shift (Fig. 10). The thermocouple's temperature reading is visually represented by a yellow and black hatched zone, indicating an overall tolerance of ± 0.5 °C. As anticipated, it is evident that the temperature data associated with the nanometre shift exhibit a higher degree of variability across all discharge conditions. The discharge at 1 C exhibits the most notable variation. Nevertheless, it is clear that the change in peak wavelength indicates the rise in temperature, which reaches its highest point at the conclusion of the discharge phase. This occurrence is observable under all discharge circumstances. The sensor consistently adheres to the temperature fall throughout the cooling phase, showing an ongoing peak nanometre change across the 2 C and 2.5 C discharge. From the linearity plots, it can be observed that the peak absorption change closely aligns with the thermocouple temperature, showing the higher level of precision in the temperature measurements. In every discharge scenario, the calculated temperature consistently matches the highest temperature achieved at the end of the discharge. It then follows the temperature decrease as the LIB cools down. Upon analysing the sensor's linearity, it was determined that the average sensitivity is −0.0072 ΔA.U./Δ°C and −0.39 Δnm/Δ°C. Moreover, the device's resolution in the specified configuration is calculated to be 1.17 °C using nanometre shift and 0.33 °C using absorption shift. This suggests that the sensor in both cases is comparable with traditional temperature sensors, such as K-Type thermocouples, which adhere to the IEC 60584–1 Class 1 standard and have a tolerance of ±1.5 °C, or IEC 60751 Class B resistance temperature sensors, which have a tolerance of ± 0.30 °C.

3.2.4. *Dynamic response*

Fig. 11 illustrates the sensor's dynamic performance concerning absorption, when the device is swiftly alternated between an ice water bath (~0.75 °C) and a hot water bath (~55 °C) to assess its adaption speed. Absorption is examined in this manner because of its superior accuracy demonstrated in battery discharge tests. The time taken for the sensor to transition from 10 % to 90 % of the stable value is used as the response time [50,63,66]. The findings indicate that transitioning from cold to hot leads in a sensor reaction time of 4.4 s, while reverting to cold yields a recovery time of 4.9 s. The findings demonstrate the sensor's capacity to detect and adjust to substantial temperature fluctuations, indicating its appropriateness for applications necessitating rapid temperature monitoring in diverse situations. Furthermore, an additional dynamic test was conducted on the sensor 18 months after its initial fabrication to evaluate its robustness and long-term stability. The sensor exhibited a cold-to-hot transition time of 4.1 s and a recovery time of

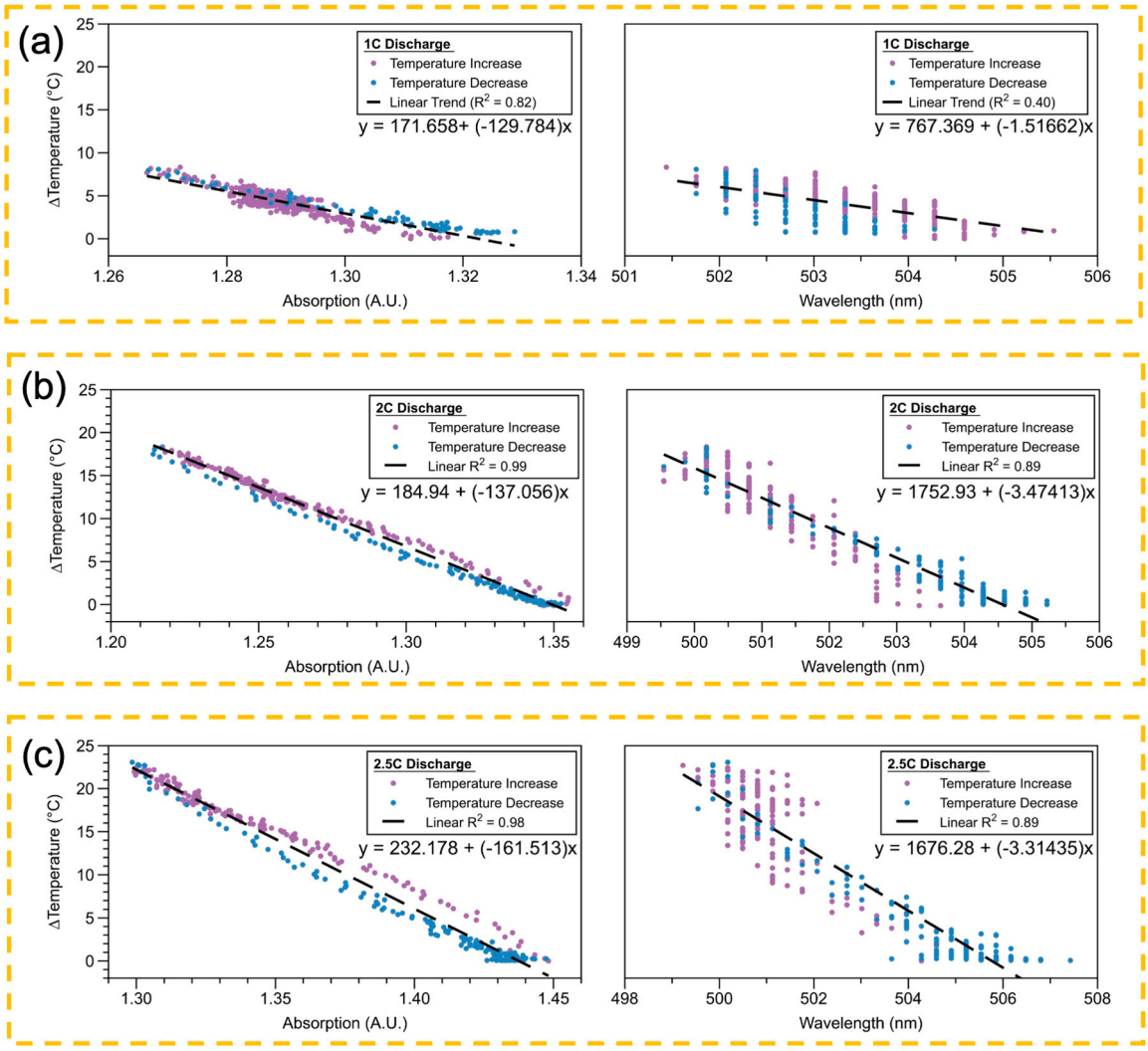

Fig. 9. Linearity Response of Sensor. (a) Linearity for 1 C discharge showing the change in absorption and peak nanometres, (b) Linearity for 2 C discharge showing the change in absorption and peak nanometres, and (c) Linearity for 2.5 C discharge showing the change in absorption and peak nanometres.

5.2 s, corresponding to deviations of –0.3 s and + 0.3 s, respectively, relative to the initial measurements. These results indicate that the sensor maintains its performance characteristics over time, underscoring the robustness of its design and fabrication.

An essential factor in enhancing sensor performance is the thickness of the PDMS layer. Minimising this thickness may improve the sensor's speed, as reduced material would require less heat absorption to trigger the refractive index alteration. This alteration may result in a swifter reaction to temperature fluctuations, thereby enhancing the sensor's overall efficiency and sensitivity. This is supported by the work presented by Xue et al. where a 1.086 μm thickness of PDMS was employed on a much more complex and expensive set up using a D-shape fibre sensor and requiring a spin coating system for fabrication. Showing a response time of ~109 ms, the authors conclude that an ultra-thin PDMS layer has a larger surface volume ratio, which can transfer heat faster to achieve rapid temperature sensing [66]. Additionally, the hysteresis results discussed in Section 3.2.3 further support the hypothesis of reduced PDMS thickness, as the shorter test durations associated with higher discharge rates provide less time for the PDMS to respond to larger temperature gradient.

When comparing the developed sensors, a U-shaped optical fibre sensor with 4.4 s (cold–hot) and 4.9 s (hot–cold) response times and sensitivities of –0.0072 A.U./°C and –0.39 nm/°C to conventional thermocouples and other published optical sensors, it stands out in several ways. Traditional thermocouples, depending on sheath thickness and environmental conditions, can achieve 63.2 % of the temperature change within milliseconds when using exposed, fine-gauge junctions, whereas thicker, sheathed variants typically up to several seconds to reach the same response level [68]; for example, response times in practical, protected thermocouples typically range from around 0.1 s to beyond 10 s, influenced by sheath thickness and environment conditions [68]. In contrast, recent fibre-optic temperature sensors, such as interferometric and Fibre Bragg Grating (FBGs) based sensors report response times from under 10 ms up to 200 s [69,70]. Additionally, U-shaped sensors published in the literature have demonstrated wavelength sensitivities from 0.07 nm/°C to the region of 1.28 nm/°C [57,71,72], and transmission loss sensitivities around 0.025 dB/°C, frequently noting increased sensitivity over straight-fibre designs [57,71]. It is difficult to determine the comparative performance of this device against other LMR devices, as it is the first U-shaped temperature sensor utilising LMR generated from PEI/GO thin-films. The dynamic response of the sensor presented in this work is slightly slower than the fastest thermocouples and some reported fibre sensors, however it is comparable to or faster than typical fibre Bragg grating sensors in practical deployment, and well within the reported range of other U-shaped fibre sensors [57,70,73], placing performance within the state-of-the-art. Furthermore, the U-shaped geometry also confers benefits in robustness and measurement flexibility versus unprotected interferometric and FBG based sensors, or

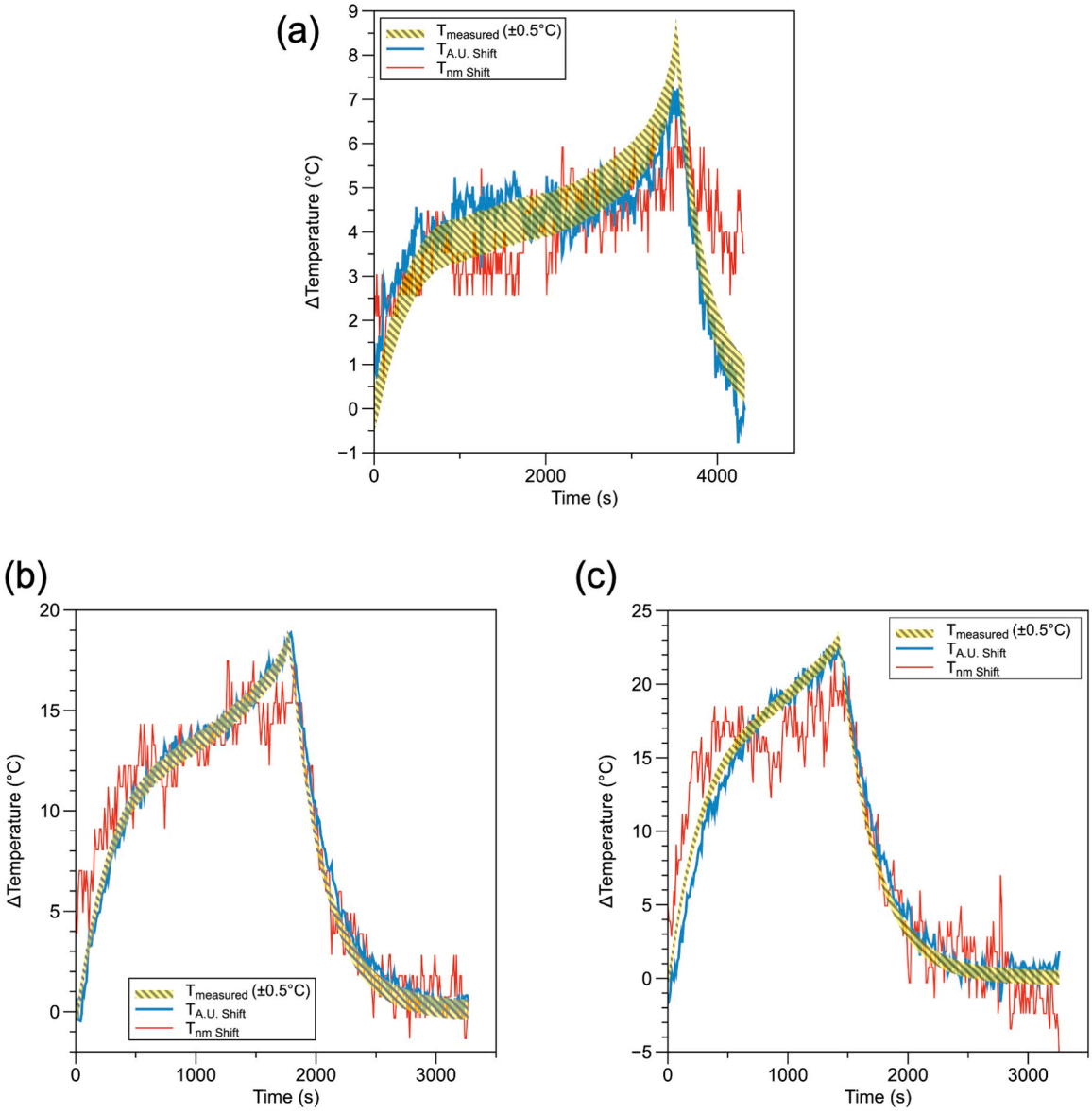

Fig. 10. Calculated Temperature of the peak absorption and shift in nanometres compared to the measured temperature ($T_{measured}$) obtained from the T-Type thermocouple, showing thermocouple error margin of ±0.5°C for discharge, (a) 1 C, (b) 2 C, and (c) 2.5 C discharge.

exposed junction thin gauge thermocouples.

The presented work achieves a favourable balance between rapid response, reliable sensitivity, and the inherent advantages of optical sensors, such as immunity to electromagnetic interference. Its performance is competitive with existing solutions, and opportunities remain to further enhance wavelength sensitivity without compromising absorption peak characteristics. A promising direction involves the development of hybrid devices that integrate the advantages of straight fibre sensors, such as well-defined resonance wavelength shifts, with the strong evanescent field interaction and high absorption sensitivity of U-shaped configurations. This approach offers a compelling route for innovation in the next generation of fibre-optic sensors.

4. Conclusion

This study has effectively showcased the first use of a lossy mode resonance optical fibre sensor for measuring temperature in energy storage systems. The sensor utilises affordable spectrometers and light sources to accurately gauge the temperature of a lithium-ion battery. This was accomplished by exploiting the theory of lossy mode resonance and employing a U-shaped fibre design which accentuated variations in absorbance rather than variations in wavelength. The achieved total sensitivity was −0.0072 A.U./°C and −0.39 nm/°C, with strong linearity values of R^2 0.98 and R^2 0.99 for the higher rated 2 C and 2.5 C, respectively. Furthermore, this work holds great significance as it demonstrates the application of lossy mode resonance optical fibre sensors in the field of electrochemical energy storage devices. This preliminary investigation is expected to highlight a new path and possibilities for the advancement of cutting-edge, innovative optical sensing devices for electrochemical energy storage, thanks to the numerous benefits of lossy mode resonance. The advantages encompass a diverse array of procedures for depositing thin-films and an extensive catalogue of materials that induce this particular resonance. The importance of this is emphasised by the continuous endeavours of researchers to develop integrated sensors that aim to improve safety, durability, and autonomy.

CRediT authorship contribution statement

Miguel Hernaez: Writing – review & editing, Supervision, Project administration, Funding acquisition, Conceptualization. **Mustehsan**

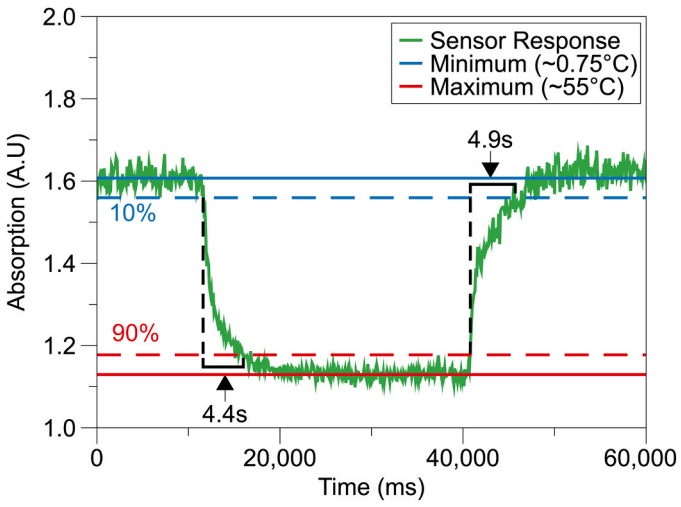

Fig. 11. Sensor dynamic response, showing heating and cooling times from 10 % to 90 %.

Beg: Formal analysis, Data curation. **Sonia Melendi-Espina:** Writing – review & editing, Supervision, Funding acquisition, Conceptualization. **Keng Goh:** Writing – review & editing, Resources. **Alcock Keith M:** Writing – original draft, Visualization, Investigation, Funding acquisition, Formal analysis, Data curation, Conceptualization.

Declaration of Competing Interest

The authors declare that they have no known competing financial interests or personal relationships that could have appeared to influence the work reported in this paper.

Acknowledgement

This work received partial support from the School of Computing, Engineering, and the Built Environment at Edinburgh Napier University through the SCEBE Internal Grant. Additionally, KMA would like to express gratitude to the Faculty of Science at the University of East Anglia for providing a scholarship (Ref:100383124) that enabled the completion of this study.

Data availability

Data will be made available on request.

References

[1] M. Gutsch, J. Leker, Global warming potential of lithium-ion battery energy storage systems: a review, J. Energy Storage 52 (2022) 105030.
[2] S. Jenu, I. Deviatkin, A. Hentunen, M. Myllysilta, S. Viik, M. Pihlatie, Reducing the climate change impacts of lithium-ion batteries by their cautious management through integration of stress factors and life cycle assessment, J. Energy Storage 27 (2020) 101023.
[3] M. Beg, K.M. Alcock, A. Titus Mavelil, D. O'Rourke, D. Sun, K. Goh, et al., Paper supercapacitor developed using a manganese dioxide/carbon black composite and a water hyacinth cellulose nanofiber-based bilayer separator, ACS Appl. Mater. Interfaces (2023).
[4] S. Dühnen, J. Betz, M. Kolek, R. Schmuch, M. Winter, T. Placke, Toward green battery cells: perspective on materials and technologies, Small Methods 4 (2020) 2000039.
[5] J. Yuan, Y. Xue, L. Liu, J. Zhang, Y. Xia, Recent development of electrode materials in semi-solid lithium redox flow batteries, J. Energy Storage 76 (2024) 109574.
[6] International Energy Agency (IEA), Global EV Outlook 2023: Catching up with climate ambitions, International Energy Agency 2023.
[7] C.R. Birkl, M.R. Roberts, E. McTurk, P.G. Bruce, D.A. Howey, Degradation diagnostics for lithium ion cells, J. Power Sources 341 (2017) 373–386.
[8] S. Ding, L. Wang, H. Dai, X. He, Prognosticating nonlinear degradation in lithium-ion batteries: operando pressure as an early indicator preceding other signals of capacity fade and safety risks, Energy Storage Mater. 75 (2025) 103998.
[9] S. Ma, M. Jiang, P. Tao, C. Song, J. Wu, J. Wang, et al., Temperature effect and thermal impact in lithium-ion batteries: a review, Progr. Nat. Sci. Mater. Int. 28 (2018) 653–666.
[10] K.M. Alcock, N. Shearer, F.V. Santos, Z. Cai, K. Goh, An innovative approach for the passive cooling of batteries: an empirical investigation of copper deposition on polyurethane foam for the enhancement of phase change material, Appl. Mater. Today 38 (2024) 102221.
[11] J. Huang, S.T. Boles, J.-M. Tarascon, Sensing as the key to battery lifetime and sustainability, Nat. Sustain. 5 (2022) 194–204.
[12] W. Mei, Z. Liu, C. Wang, C. Wu, Y. Liu, P. Liu, et al., Operando monitoring of thermal runaway in commercial lithium-ion cells via advanced lab-on-fiber technologies, Nat. Commun. 14 (2023) 5251.
[13] E. Miele, W.M. Dose, I. Manyakin, M.H. Frosz, Z. Ruff, M.F.L. De Volder, et al., Hollow-core optical fibre sensors for operando Raman spectroscopy investigation of Li-ion battery liquid electrolytes, Nat. Commun. 13 (2022) 1651.
[14] H. Wang, B. Zhang, S. Che, K. Wang, Advances in the application of fiber optic sensors for high spatial resolution monitoring of Lithium-Ion batteries, ACS Appl. Electron. Mater. 7 (2025) 5743–5756.
[15] L. Wang, Y. Wang, J. Wang, F. Li, A high spatial resolution FBG sensor array for measuring ocean temperature and depth, Photon. Sens. 10 (2020) 57–66.
[16] S. Liu, P. Zhu, F. Xie, M.A. Soto, Gecko-inspired self-adhesive packaging for strain-free temperature sensing based on optical fibre bragg gratings, Sci. Rep. 13 (2023) 4148.
[17] M. Elsherif, A.E. Salih, M.G. Muñoz, F. Alam, B. AlQattan, D.S. Antonysamy, et al., Optical fiber sensors: working principle, applications, and limitations, Adv. Photonics Res. 3 (2022) 2100371.
[18] K.M. Alcock, Á. González-Vila, M. Beg, F. Vedreño-Santos, Z. Cai, L.S.M. Alwis, et al., Individual Cell-Level temperature monitoring of a Lithium-Ion battery pack, Sensors 23 (2023).
[19] Y. Wu, X. Long, J. Lu, R. Zhou, L. Liu, Y. Wu, Long-life in-situ temperature field monitoring using fiber bragg grating sensors in electromagnetic launch high-rate hardcase lithium-ion battery, J. Energy Storage 57 (2023) 106207.
[20] K.M. Alcock, M. Grammel, Á. González-Vila, L. Binetti, K. Goh, L.S.M. Alwis, An accessible method of embedding fibre optic sensors on lithium-ion battery surface for in-situ thermal monitoring, Sens. Actuators A Phys. 332 (2021).
[21] J. Bonefacino, S. Ghashghaie, T. Zheng, C.-P. Lin, W. Zheng, L.A. Blanquer, et al., High-Fidelity strain and temperature measurements of Li-Ion batteries using polymer optical fiber sensors, J. Electrochem. Soc. 169 (2022) 100508.
[22] J. Peng, S. Jia, S. Yang, X. Kang, H. Yu, Y. Yang, State estimation of lithium-ion batteries based on strain parameter monitored by fiber bragg grating sensors, J. Energy Storage 52 (2022) 104950.
[23] Z. Miao, Y. Li, X. Xiao, Q. Sun, B. He, X. Chen, et al., Direct optical fiber monitor on stress evolution of the sulfur-based cathodes for lithium–sulfur batteries, Energy Environ. Sci. (2022) 2029–2038.
[24] Y. Li, Y. Zhang, Z. Li, Z. Yan, Xiangpeng Xiao, X. Liu, et al., Operando decoding of surface strain in Anode-Free lithium metal batteries via optical fiber sensor, Adv. Sci. 9 (2022) 2203247.
[25] X. Han, H. Zhong, K. Li, X. Xue, W. Wu, N. Hu, et al., Operando monitoring of dendrite formation in lithium metal batteries via ultrasensitive tilted fiber bragg grating sensors, Light Sci. Appl. 13 (2024) 24.
[26] J. Hu, H. Huang, M. Bai, T. Zhan, Z. Yang, Y. Yu, et al., A high sensitive fiber-optic strain sensor with tunable temperature sensitivity for temperature-compensation measurement, Sci. Rep. 7 (2017) 42430.
[27] K.M. Alcock, M. Grammel, L. Binetti, Á. González-Vila, K. Goh, L.S.M. Alwis, Feasibility study on the potential of fibre bragg gratings for thermal monitoring of cylindrical lithium-ion batteries, in: G.W.A.D.M. Cranch, P. Dragic (Eds.), Optical Fiber Sensors Conference 2020 Special Edition, Optical Society of America, Washington, DC, 2020 p. T3.49.
[28] J. Fleming, T. Amietszajew, E. McTurk, D. Greenwood, R. Bhagat, Development and evaluation of in-situ instrumentation for cylindrical Li-ion cells using fibre optic sensors, Hardwarex 3 (2018) 100–109.
[29] E. McTurk, T. Amietszajew, J. Fleming, R. Bhagat, Thermo-electrochemical instrumentation of cylindrical Li-ion cells, J. Power Sources 379 (2018) 309–316.
[30] H. Chikh-Bled, K. Chah, A. Gonzalez-Vila, B. Lasri, C. Caucheteur, Behavior of femtosecond laser-induced eccentric fiber Bragg gratings at very high temperatures, Opt. Lett. 41 (2016) 4048–4051.
[31] Á. González-Vila, A. Ioannou, M. Loyez, M. Debliquy, D. Lahem, C. Caucheteur, Surface plasmon resonance sensing in gaseous media with optical fiber gratings, Opt. Lett. 43 (2018) 2308.
[32] K. Seitkamal, B. Kudaibergenov, A. Dauletova, M. Sypabekova, Y. Amerzhanova, A. Rakhimbekova, et al., Proof of principle for a sensitive, real time and label-free detection of poxviruses using optical fiber biosensors, Optik 288 (2023) 171195.
[33] J. Bonefacino, S. Ghashghaie, T. Zheng, High-fidelity strain and temperature measurements of li-ion batteries using polymer optical fiber sensors, J. Electrochem. Soc. (2022).
[34] P. Sanchez, C.R. Zamarreño, M. Hernaez, I.R. Matias, F.J. Arregui, Optical fiber refractometers based on lossy mode resonances by means of SnO2 sputtered coatings, Sens. Actuators B Chem. 202 (2014) 154–159.
[35] I.D. Villar, C.R. Zamarreno, M. Hernaez, F.J. Arregui, I.R. Matias, Lossy mode resonance generation with Indium-Tin-Oxide-Coated optical fibers for sensing applications, J. Light. Technol. 28 (2010) 111–117.
[36] I.D. Villar, C.R. Zamarreño, P. Sanchez, M. Hernaez, C.F. Valdivielso, F.J. Arregui, et al., Generation of lossy mode resonances by deposition of high-refractive-index coatings on uncladded multimode optical fibers, J. Opt. 12 (2010) 095503.

[37] C.R. Zamarreño, M. Hernáez, I. Del Villar, I.R. Matías, F.J. Arregui, Optical fiber ph sensor based on lossy-mode resonances by means of thin polymeric coatings, Sens. Actuators B Chem. 155 (2011) 290–297.
[38] I. Del Villar, F.J. Arregui, C.R. Zamarreño, J.M. Corres, C. Bariain, J. Goicoechea, et al., Optical sensors based on lossy-mode resonances, Sens. Actuators B Chem. 240 (2017) 174–185.
[39] A.B. Socorro, I.D. Villar, J.M. Corres, F.J. Arregui, I.R. Matias, Tapered Single-Mode optical fiber ph sensor based on lossy mode resonances generated by a polymeric thin-film, IEEE Sens. J. 12 (2012) 2598–2603.
[40] L. Zhao, H. Zhang, N.H. Kim, D. Hui, J.H. Lee, Q. Li, et al., Preparation of graphene oxide/polyethyleneimine layer-by-layer assembled film for enhanced hydrogen barrier property, Compos. Part B Eng. 92 (2016) 252–258.
[41] E.E.G. Martínez, I.R. Matías, S. Melendi-Espina, M. Hernáez, C.R. Zamarreño, Lossy mode resonance based 1-butanol sensor in the mid-infrared region, Sens. Actuators B Chem. 388 (2023) 133845.
[42] M. Divagar, A. Gowri, S. John, V.V.R. Sai, Graphene oxide coated U-bent plastic optical fiber based chemical sensor for organic solvents, Sens. Actuators B Chem. 262 (2018) 1006–1012.
[43] P. Zubiate, A. Urrutia, C.R. Zamarreño, J. Egea-Urra, J. Fernández-Irigoyen, A. Giannetti, et al., Fiber-based early diagnosis of venous thromboembolic disease by label-free D-dimer detection, Biosens. Bioelectron. X 2 (2019) 100026.
[44] P. Zubiate, C.R. Zamarreño, P. Sánchez, I.R. Matias, F.J. Arregui, High sensitive and selective C-reactive protein detection by means of lossy mode resonance based optical fiber devices, Biosens. Bioelectron. 93 (2017) 176–181.
[45] A. Ozcariz, C.R. Zamarreño, P. Zubiate, F.J. Arregui, Is there a frontier in sensitivity with lossy mode resonance (LMR) based refractometers? Sci. Rep. 7 (2017) 10280.
[46] J. Xiao, X. Li, W.-M. Zhao, Q. Wang, Lossy mode resonance sensor modified with TiO2/PSS&Au-nanoparticles bilayers for highly sensitive refractive index sensing, Opt. Fiber Technol. 68 (2022) 102735.
[47] M. Hernaez, A.G. Mayes, S. Melendi-Espina. Sensitivity enhancement of lossy mode resonance-based ethanol sensors by graphene oxide coatings, IEEE SENSORS, IEEE, 2017, pp. 1–3.
[48] P.I. Kuznetsov, D.P. Sudas, E.A. Savelyev, Fiber optic lossy mode resonance based sensor for aggressive liquids, Sens. Actuators A Phys. 321 (2021) 112576.
[49] Jyoti Kavita, S.K. Mishra, A.K. Mishra, K.P. Misra, R.K. Verma, Detection of alcohol content in food products by lossy mode resonance technique, J. Electrochem. Soc. 169 (2022) 077504.
[50] M. Hernaez, B. Acevedo, A.G. Mayes, S. Melendi-Espina, High-performance optical fiber humidity sensor based on lossy mode resonance using a nanostructured polyethylenimine and graphene oxide coating, Sens. Actuators B Chem. 286 (2019) 408–414.
[51] P. Sanchez, C.R. Zamarreño, M. Hernaez, I. Del Villar, C. Fernandez-Valdivielso, I. R. Matias, et al., Lossy mode resonances toward the fabrication of optical fiber humidity sensors, Meas. Sci. Technol. 23 (2012) 014002.
[52] P. Zubiate, C.R. Zamarreño, I. Del Villar, I.R. Matias, F.J. Arregui, Tunable optical fiber ph sensors based on TE and TM lossy mode resonances (LMRs), Sens. Actuators B Chem. 231 (2016) 484–490.
[53] I. Vitoria, E.E. Gallego, S. Melendi-Espina, M. Hernaez, C. Ruiz Zamarreño, I. R. Matías, Gas sensor based on lossy mode resonances by means of thin graphene oxide films fabricated onto planar coverslips, Sensors 23 (2023).
[54] S.P. Usha, S.K. Mishra, B.D. Gupta, Fiber optic hydrogen sulfide gas sensors utilizing ZnO thin film/ZnO nanoparticles: a comparison of surface plasmon resonance and lossy mode resonance, Sens. Actuators B Chem. 218 (2015) 196–204.
[55] S.K. Mishra, S.P. Usha, B.D. Gupta, A lossy mode resonance-based fiber optic hydrogen gas sensor for room temperature using coatings of ITO thin film and nanoparticles, Meas. Sci. Technol. 27 (2016) 045103.
[56] M. Szymański, K. Kosiel, R. Huk, K. Gajowniczek, LMR: a software for modeling and reverse optimization of straight-core lossy mode resonance (LMR) based sensors, Expert Syst. Appl. 251 (2024) 123925.
[57] Y.-L. Chou, H.-Y. Wen, Y.-Q. Weng, Y.-C. Liu, C.-W. Wu, H.-C. Hsu, et al., A U-Shaped optical fiber temperature sensor coated with electrospinning polyvinyl alcohol nanofibers: simulation and experiment, Polymers (2022).
[58] P. Vikas, Saccomandi, Design considerations of an ITO-coated U-shaped fiber optic LMR biosensor for the detection of antibiotic ciprofloxacin, Biosensors (2023).
[59] C.-S. Park, K.-I. Joo, S.-W. Kang, H.-R. Kim, A PDMS-Coated optical fiber bragg grating sensor for enhancing temperature sensitivity, J. Opt. Soc. Korea 15 (2011) 329–334.
[60] O. Fuentes, J.M. Corres, I. Domínguez, I.D. Villar, I.R. Matias, Lossy mode resonances generated in planar configuration for two-parameter sensing, IEEE Sens. J. 22 (2022) 11264–11270.
[61] Z. Zhu, L. Liu, Z. Liu, Y. Zhang, Y. Zhang, Surface-plasmon-resonance-based optical-fiber temperature sensor with high sensitivity and high figure of merit, Opt. Lett. 42 (2017) 2948–2951.
[62] N. Paliwal, N. Punjabi, J. John, S. Mukherji, Design and fabrication of lossy mode resonance based U-Shaped fiber optic refractometer utilizing dual sensing phenomenon, J. Light. Technol. 34 (2016) 4187–4194.
[63] M. Hernaez, A.G. Mayes, S. Melendi-Espina, Graphene oxide in lossy mode Resonance-Based optical fiber sensors for ethanol detection, Sensors 18 (2018).
[64] M. Hernaez, A.G. Mayes, S. Melendi-Espina, Lossy mode resonance generation by graphene oxide coatings onto cladding-removed multimode optical fiber, IEEE Sens. J. 19 (2019) 6187–6192.
[65] V. Kandjou, M. Hernaez, B. Acevedo, S. Melendi-Espina, Interfacial crosslinked controlled thickness graphene oxide thin-films through dip-assisted layer-by-layer assembly means, Prog. Org. Coat. 137 (2019) 105345.
[66] Y. Xue, J. Yang, P. Ye, B. Li, S. Gao, Y. Liu, et al., High-sensitivity fiber temperature sensor based on composite film structure and lossy mode resonance, Opt. Laser Technol. 181 (2025) 111998.
[67] F.U. Hernandez, T. Wang, S.-W. Lee, A. Norris, L. Liu, B.R. Hayes-Gill, et al., U-shape functionalized optical fibre sensors for measurement of anaesthetic propofol, Sens. Actuators B Chem. 372 (2022) 132653.
[68] Sab-Cables, Response time mineral insulated thermocouples and resistance thermometers, 2025.
[69] J.M. Coote, R. Torii, A.E. Desjardins, Dynamic characterisation of fibre-optic temperature sensors for physiological monitoring, Sensors 21 (2021).
[70] H. Wang, C. Li, L. Liang, K. Jiang, S. Dai, H. Wu, et al., Fast response characteristics of fiber bragg grating temperature sensors and explosion temperature measurement tests, Sens. Actuators A Phys. 354 (2023) 114236.
[71] Y. Zhang, P. Huang, W. Li, Z. Huang, X. Tang, Z. Liu, et al., U-shaped MZI optical fiber temperature sensor based on PDMS sensitization, Opt. Fiber Technol. 93 (2025) 104252.
[72] R.K. Gangwar, S. Kumari, A.K. Pathak, S.D. Gutlapalli, M.C. Meena, Optical fiber based temperature sensors: a review, Optics (2023) 171–197.
[73] Y. Zhao, S.-q Zhang, Y. Peng, L. Cai, C.-f Li, X.-m Chen, et al., A taper-enhanced U-shaped hybrid fiber optic sensor based on SPR and MZI for simultaneous measurement of salinity and temperature, Sens. Actuators B Chem. 441 (2025) 138001.

Keith M. Alcock received his BEng (Hons) degree in Energy & Environmental Engineering in 2015 and his master degree in Renewable Energy in 2016, both from Edinburgh Napier University, UK. In 2023 at the same institution he completed a PhD in Engineering, focusing on lithium-ion battery thermal management utilising foam and phase change materials in 2023. He is currently pursuing a second PhD from the University of East Anglia in Lossy Mode Resonance (LMR) optical fibre sensors for energy storage applications.

Keng Goh graduated with BEng (Hons) degree in Electrical & Electronic and PhD in Nonlinear Control system application from University of Leicester in 1998 and 2004 respectively. In between these studies, he worked with Hewlett Packard for two years as instrumentation engineer. He is currently a lecturer at Edinburgh Napier University.

Mustehsan Beg recently completed his PhD thesis at Edinburgh Napier University on flexible energy storage devices, with most of his work focused on the processing of water hyacinth cellulose nanofibers and the synthesis of functional materials such as cellulose-based separators, hydrogels for flexible and wearable energy harvesting and electro-chemical energy storage devices. Previous work experience includes being a simulation engineer, and modelling and simulating battery packs for hydrogen fuel cell vehicles for HVS systems.

Sonia Melendi-Espina holds an MEng in Chemical Engineering from the University of Oviedo (Spain) and a PhD from the Carbon Science and Technology Institute (INCAR-CSIC, Spain). She joined the University of East Anglia (UK) as a Lecturer in Engineering in 2014 and was promoted to Associate Professor in Energy and Environmental Engineering in 2019. Her research focuses on the chemistry and engineering of carbon materials, particularly the development and processing of functionalised carbon nanomaterials for applications in energy, chemical engineering, and environmental technologies. She has extensive expertise in their synthesis, functionalisation, characterisation, deposition, processing, and handling. At the University of East Anglia, she has established her own research group, fostering multidisciplinary collaborations in areas such as composite materials, energy storage, water purification membranes, and sensors.

Miguel Hernaez received his M.Sc. degree in Telecommunications Engineering from Universidad Pública de Navarra (Pamplona, Spain) in 2009, followed by a Ph.D. from the same institution in 2011. During his doctoral studies, he developed a strong interest in the design and fabrication of optical fibre sensors based on nanostructured coatings. In 2016, he joined the University of East Anglia (Norwich, U.K.) as a Marie Skłodowska-Curie Research Fellow, where his work focused on the development of optical fibre sensors functionalized with molecularly imprinted polymers. Since September 2018, he has held the position of Lecturer in Electronic and Electrical Engineering at UEA. His research interests are primarily centred on optical fibre sensing technologies, with particular emphasis on applications in the field of energy storage and the integration of graphene-based materials.